

Enabling Thin and Flexible Solid-State Composite Electrolytes by the Scalable Solution Process

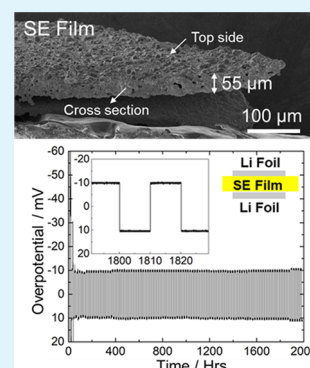
Darren H. S. Tan,[†] Abhik Banerjee,[†] Zhi Deng,[†] Erik A. Wu,[†] Han Nguyen,[†] Jean-Marie Doux,[†] Xuefeng Wang,[†] Ju-hsiang Cheng,[†] Shyue Ping Ong,^{†,‡,§} Ying Shirley Meng,^{*,†,‡,§} and Zheng Chen^{*,†,‡,§}

[†]Department of NanoEngineering, [‡]Sustainable Power & Energy Center (SPEC), and [§]Program of Chemical Engineering, University of California, San Diego, La Jolla, California 92093, United States

Supporting Information

ABSTRACT: All solid-state batteries (ASSBs) have the potential to deliver higher energy densities, wider operating temperature range, and improved safety compared with today's liquid-electrolyte-based batteries. However, of the various solid-state electrolyte (SSE) classes—polymers, sulfides, or oxides—none alone can deliver the combined properties of ionic conductivity, mechanical, and chemical stability needed to address scalability and commercialization challenges. While promising strategies to overcome these include the use of polymer/oxide or sulfide composites, there is still a lack of fundamental understanding between different SSE–polymer–solvent systems and its selection criteria. Here, we isolate various SSE–polymer–solvent systems and study their molecular level interactions by combining various characterization tools. With these findings, we introduce a suitable Li₇P₃S₁₁SSE–SEBS polymer–xylene solvent combination that significantly reduces SSE thickness (~50 μm). The SSE–polymer composite displays high room temperature conductivity (0.7 mS cm⁻¹) and good stability with lithium metal by plating and stripping over 2000 h at 1.1 mAh cm⁻². This study suggests the importance of understanding fundamental SSE–polymer–solvent interactions and provides a design strategy for scalable production of ASSBs.

KEYWORDS: composite electrolytes, interfacial engineering, high stability, solid-state batteries, scalable manufacturing



INTRODUCTION

All-solid-state batteries (ASSBs) are regarded as the future energy storage technology to replace the state-of-the-art liquid-electrolyte-based batteries due to their improved safety from the use of nonflammable electrolytes, lower costs of production, and the ability to operate over a wide range of temperatures.^{1,2} The use of solid-state electrolytes (SSEs) is also believed to be able to address lithium dendrite growth problems, enabling the use of metallic lithium as the anode with a reduced risk of short circuit in the battery.^{3,4} However, despite their widely recognized benefits, ASSBs are unlikely to compete with conventional batteries unless they can meet combined SSE requirements such as high ionic conductivity, suitable mechanical property, good electrochemical stability needed for scalable processability, and high performance.^{5–7}

Methods to produce conventional batteries on a large scale are well established; however, because of the air/moisture sensitivities and poor mechanical properties of sulfide- or oxide-based electrolytes, it is challenging to adopt the conventional slurry casting assembly setup for ASSBs manufacturing.^{6,8} In terms of energy density, ASSBs still remain inferior to conventional batteries due to the thick SSEs used to compensate for poor mechanical properties in its pelletized form.^{9,10} Most reports on ASSBs utilize sulfide or oxide electrolyte layers ranging from 0.6 to 1.2 mm, vastly

reducing the weight fraction of active materials in the cells, keeping their overall energy density low.^{2,11–13} The thickness of electrolyte layers needs to be reduced by at least an order of magnitude for ASSBs to compete with conventional batteries in terms of energy density. Physical vapor deposition (PVD), pulsed laser deposition (PLD), and sputtering have been explored in some cases to fabricate SSE with reduced thicknesses,^{2,6,14} but solvent-based techniques such as solution casting used in conventional batteries remain most attractive from a manufacturing point of view. To address these limitations, using flexible composite solid electrolytes by combining inorganic Li⁺ superionic conductors and polymers has been considered a promising approach. Recent reports of oxide-based composite electrolytes such as Li₇La₃Zr₂O₁₂ (LLZO) with poly(ethylene oxide) (PEO)^{15,16} and LiAlGePO₄ (LAGP) class ceramics with poly(vinylidene fluoride) (PVDF)¹⁷ in ASSBs have generated interest for new types of composite electrolytes, relying on their mechanical flexibility and ability to form thin films with good electrochemical stability. Compared to their oxide-based counterparts, relatively few have reported the use of composite sulfide–

Received: June 5, 2019

Accepted: August 9, 2019

Published: August 9, 2019

polymer electrolytes to address cell energy density and processability problems because of their chemical instability.^{17–22} Among the literatures on sulfides ($\text{Li}_6\text{PS}_5\text{Cl}/\text{Li}_3\text{PS}_4$) with polymers (acrylonitrile butadiene (NBR)/polyvinylpyrrolidone (PVP)), promising electrochemical results on composite conductivity and cell performance have been reported (Table S1).^{20–22} However, there is still a limited understanding of how sulfide electrolytes behave and how they interact with various functional moieties in both polymers and solvents. This knowledge is key toward developing successful composite electrolytes.

In this work, we developed a scalable method to synthesize thin, flexible, and electrochemically stable sulfide-based composite electrolytes with high room-temperature Li^+ conductivities. We hypothesize that an inert chemical environment needs to be created and maintained for sulfide species throughout the solution process. This will suppress the high reactivity of sulfides in the presence of solvents and polymers, which can preserve the intrinsic high conductivity of sulfide electrolytes. Our strategy was to systematically investigate their electrochemical properties and interactions with solvents and polymers to elucidate how sulfide solid electrolytes behave with a variety of functional moieties. This was done by applying both bulk and surface sensitive characterization tools to different sulfide–solvent and sulfide–polymer mixtures to probe their respective chemical compatibilities. Furthermore, we examined their relative stability in air and demonstrate the potential use of hydrophobic polymers to improve its moisture stability. Our understanding led to rationale designs of organic/inorganic composite SSE that are found to be stable against lithium metal and show significantly improved chemical stability in air compared with the original sulfide solid electrolyte. This work provides a promising approach toward scalable manufacturing of composite electrolytes to realize high-energy ASSBs.

RESULTS AND DISCUSSION

SSE Material Considerations. An ideal SSE must meet several key requirements: (1) low overall ionic resistance at room temperature, (2) small thickness to minimize electrolyte vol %, (3) high mechanical robustness to withstand deformation, and (4) good electrochemical stability versus metallic lithium.^{23,24} Considering these criteria, $\text{Li}_7\text{P}_3\text{S}_{11}$ would be an ideal candidate for this study. The glass ceramic $\text{Li}_7\text{P}_3\text{S}_{11}$ is also known to deliver high room temperature ionic conductivity (up to 1.3 mS/cm) by a simple cold press.²⁵ Although the electrochemical stability window of $\text{Li}_7\text{P}_3\text{S}_{11}$ is narrow, various studies have found interfacial decomposition products to have ideal properties of ionic conductivity and interface passivation.^{25–27} Additionally, $\text{Li}_7\text{P}_3\text{S}_{11}$ is a unique glass ceramic SSE that contains various lithium thiophosphates ($\text{P}_2\text{S}_7^{4-}$, $\text{P}_2\text{S}_6^{4-}$, and PS_4^{3-}) within its chemical structure, allowing effective characterization of any degradation in its various units. In this work, we first synthesized $\text{Li}_7\text{P}_3\text{S}_{11}$ powder, which showed expected crystal structure, chemical composition, and intrinsic electrochemical properties (Figures S1–S4). The as-synthesized SSE powders were used to prepare composite electrolytes.

Polymer and Solvent Material Considerations. Considering the chemical reactivities of sulfide electrolytes, we must account for potential interactions that might arise between the sulfides and the polymers or solvents. Given that chemical properties of polymers are largely dependent on

their functional groups, four types of polymers with different functional groups are chosen for our investigation, including PEO, poly(vinylidene fluoride)-*co*-hexafluoropropylene (PVDF-HFP), NBR, and polystyrene-*block*-polyethylene-*ran*-butylene-*block*-polystyrene (SEBS). These polymers have been commonly used in battery fabrication.^{20,21,28–31} Additionally, their distinct functional groups containing oxygen, fluorine, or nitrogen make them good candidates for this study (Figure S5). SEBS is a polymer that is comprised of only carbon and hydrogen groups, representing another type of chemically inert polymer for comparison. The solvents acetonitrile (ACN), dimethyl carbonate (DMC), toluene (TOL), and *p*-xylene (XYL) are chosen based on their ability to dissolve the selected polymers (Figure S6). The polymer–solvent pair selections are summarized in Table S2. Solid $\text{Li}_7\text{P}_3\text{S}_{11}$ /polymer composite electrolyte films were synthesized by using the solution slurry casting method. To understand the SSE–polymer–solvent behavior and their selection criteria for synthesizing thin flexible electrolyte films, we first isolated the effects of each SSE–solvent and SSE–polymer mixtures and studied their chemical and electrochemical compatibilities.

$\text{Li}_7\text{P}_3\text{S}_{11}$ –Solvent Compatibility. To examine the solvent effects on the electrolyte, common solvents such as water, methyl ethyl ketone (MEK), tetrahydrofuran (THF), *N*-methyl-2-pyrrolidone (NMP), dimethylformamide (DMF), ACN, DMC, TOL, and XYL were first used for $\text{Li}_7\text{P}_3\text{S}_{11}$ dispersions. Various color changes were observed as seen in Figure 1. While NMP and DMF solutions turned dark green

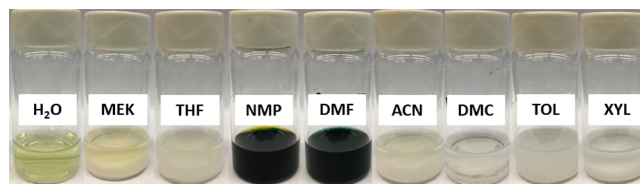


Figure 1. Different solvent color changes after addition of $\text{Li}_7\text{P}_3\text{S}_{11}$.

and blue, respectively, MEK, THF, and ACN solutions turned yellow initially before settling to a yellowish-white color. This is an indication of chemical degradation of $\text{Li}_7\text{P}_3\text{S}_{11}$ when exposed to these solvents. To characterize these degradations, solvents were removed, and their precipitates were collected for XRD, Raman, and XPS analyses. Only electrolyte precipitates obtained from ACN, DMC, TOL, and XYL dispersions were selected for characterization as they were solvents used to dissolve the respective polymers.

As shown in Figure 2, the XRD patterns of solutes derived from ACN and DMC solutions no longer matched that of the pristine $\text{Li}_7\text{P}_3\text{S}_{11}$. The crystal structure of $\text{Li}_7\text{P}_3\text{S}_{11}$ has completely degraded, evident from the absence of main peaks in the pristine pattern. It is difficult to determine the specific degradation products formed from just the XRD patterns as it is likely a mixture of various phosphorus and sulfide derivatives in both crystalline and amorphous phases. Conversely, patterns derived from the TOL and XYL dispersions (Figure 2b) remain unchanged compared to the pristine pattern, indicating the feasibility of using these solvents to retain the crystalline structure of $\text{Li}_7\text{P}_3\text{S}_{11}$ during the solution mixing process.

The Raman spectra in Figure 3a reaffirm findings in the XRD study, where precipitates derived from TOL and XYL dispersions were able to retain the characteristic Raman modes

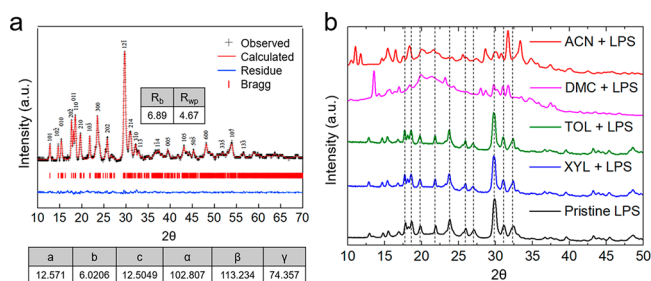


Figure 2. (a) Rietveld refinement of pristine $\text{Li}_7\text{P}_3\text{S}_{11}$; the refinement model was adapted from the literature.³² (b) XRD patterns of $\text{Li}_7\text{P}_3\text{S}_{11}$ after dispersion in ACN, DMC, TOL, and XYL.

of pristine $\text{Li}_7\text{P}_3\text{S}_{11}$ (Figure 3b), while precipitates from ACN and DMC dispersions were distinctly different. Relative intensities of the main conduction modes $\text{P}_2\text{S}_7^{4-}$ (406 cm^{-1}) decreased while PS_4^{3-} (420 cm^{-1}) and $\text{P}_2\text{S}_6^{4-}$ (385 cm^{-1}) increased significantly. The result indicates that the dispersion of SSE in ACN and DMC solvents favors decomposition of $\text{Li}_7\text{P}_3\text{S}_{11}$, generating the undesired products. There was also an unknown product shown at the wavelength of 430 cm^{-1} for solute from the ACN dispersion which requires additional analysis to identify. According to the XRD and Raman analyses, there are significant changes to both bulk and local structures of electrolyte dispersed in ACN and DMC solvent compared to pristine $\text{Li}_7\text{P}_3\text{S}_{11}$. To identify any additional specific decomposition products, X-ray photoelectron spectroscopy (XPS) was conducted on all precipitates, and combined XPS binding energies are plotted in Figure 3c. As the binding energies of various phosphorus and sulfur products are similar, with energies of $\text{P}_2\text{S}_7^{4-}$ and $\text{P}_2\text{S}_6^{4-}$ overlapping at 161.5 eV , it was difficult to deconvolute these products from the peak patterns. However, it was observed that peak shapes of solutes from ACN and DMC dispersions were blue-shifted in the phosphorus region (Figure 3c), indicating an increased amount of PS_4^{3-} mode, consistent with the Raman analysis. Additionally, the XPS analysis also showed no phosphate or sulfate products present. This suggests that solvent-induced degradation of $\text{Li}_7\text{P}_3\text{S}_{11}$ was not a result of any chemical

reaction with the solvents containing oxygen/nitrogen groups but due to the degradation of the $\text{Li}_7\text{P}_3\text{S}_{11}$ itself, forming decomposed products such as $\text{P}_2\text{S}_6^{4-}$ and PS_4^{3-} . This likely occurs from a partial or complete dissolution of pristine $\text{Li}_7\text{P}_3\text{S}_{11}$ in certain solvents and the subsequent reaction forming undesired Li/P/S derivatives after the solvents were removed. These findings agree with existing solution-based synthesis methods of sulfide SSEs, where solvents such as ACN are used in the dissolution and precipitation of precursors followed by heat treatment during the synthesis process.^{33–35}

To better understand the relationship between $\text{Li}_7\text{P}_3\text{S}_{11}$ and the respective solvents, we can compare the solvent relative properties using their polarity indexes and dielectric constants. From Table 1, one can identify a qualitative trend between the solvent polarity and its degradative effect on $\text{Li}_7\text{P}_3\text{S}_{11}$, consistent with some reported literature.^{20,36} However, this trend is more pronounced when dielectric constants are considered. As the dielectric constant of the solvent increases, a greater degree of degradation was observed visually through their color changes as well as based on the above XRD, Raman, and XPS analyses. To further analyze solvent polarity and dielectric constant effects, computational methods were used to examine their molecular level interactions.

Computational DFT Calculations of Molecular Interactions. Using DFT calculations, we find that the solvation free energies of $\text{P}_2\text{S}_7^{4-}$ become more favorable as the dielectric constant of solvent increases (Figure 4a), indicating that these components are more likely to dissolve in polar solvents with high dielectric constants. In addition, reaction energies were calculated for two reactions involving $\text{P}_2\text{S}_7^{4-}$, the characteristic building unit of $\text{Li}_7\text{P}_3\text{S}_{11}$: $2e^- + \text{P}_2\text{S}_7^{4-} \rightarrow \text{P}_2\text{S}_6^{4-} + \text{S}^{2-}$ (reaction A) and $\text{P}_2\text{S}_7^{4-} + \text{S}^{2-} \rightarrow 2\text{PS}_4^{3-}$ (reaction B). Reaction A forming $\text{P}_2\text{S}_6^{4-}$ and S^{2-} becomes highly favorable as the dielectric constant of solvent increases (Figure 4b). This explains the experimental observation of increased $\text{P}_2\text{S}_6^{4-}$ after mixing $\text{Li}_7\text{P}_3\text{S}_{11}$ in solvents such as ACN with larger dielectric constant (Figure 3a). In contrast, reaction B between $\text{P}_2\text{S}_7^{4-}$ and the S^{2-} intermediate to form PS_4^{3-} is more favorable for solvents with lower dielectric constants (e.g., <10) and remains relatively constant for solvents with dielectric constants >10 .

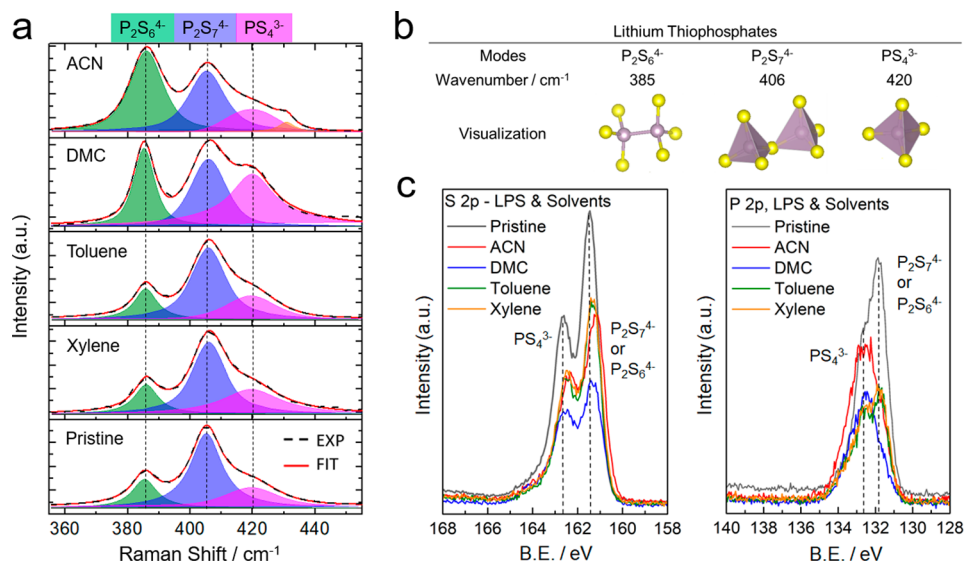
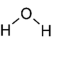
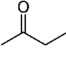

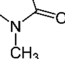
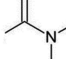
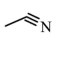
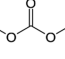
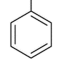
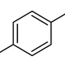


Figure 3. (a) Deconvoluted Raman spectra of $\text{Li}_7\text{P}_3\text{S}_{11}$ after dispersion in different solvents. (b) Visualizations of detected lithium thiophosphates present. (c) XPS spectra of 2p regions of sulfur and phosphorus showing the combined binding energies of $\text{Li}_7\text{P}_3\text{S}_{11}$ after dispersion.

Table 1. Common Solvents Used in Battery Materials and Their Polarities and Dielectric Constants. “Nil” Indicates No Color Change Observed.

Solvent	Water	MEK	THF	NMP	DMF	ACN	DMC	TOL	XYL
Polarity Index	10.2	4.7	4	6.7	6.4	5.8	4.7	2.4	2.5
Dielectric Constant	80.1	18.2	7.5	32.3	37.2	35.7	3.1	2.4	2.3
Structure									
Color on Mix	Light Yellow	Yellow White	Yellow White	Dark Green	Dark Blue	Yellow White	Nil	Nil	Nil

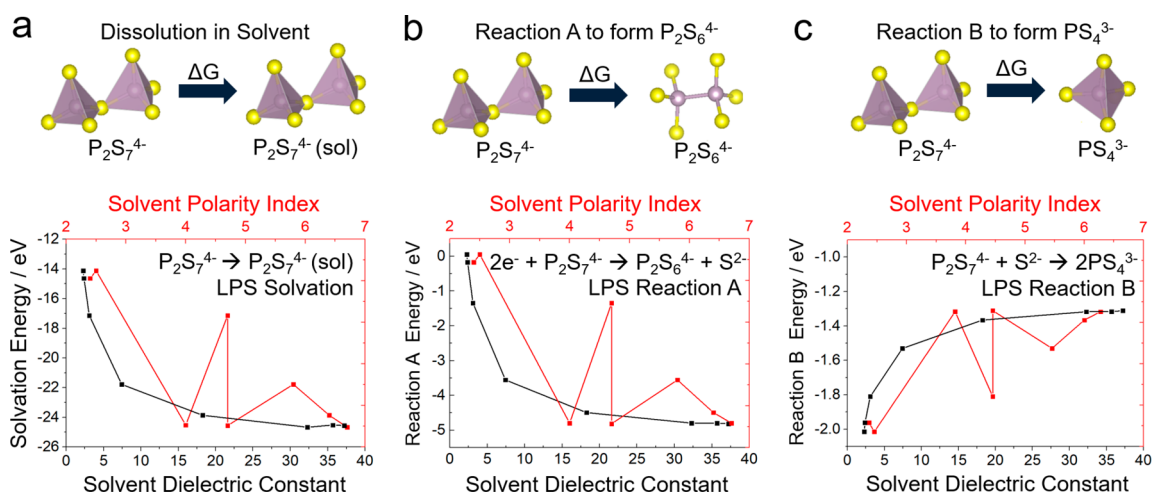


Figure 4. $\text{Li}_7\text{P}_3\text{S}_{11}$ -solvent degradation mechanism vs solvent polarity/dielectric constant: (a) $\text{P}_2\text{S}_7^{4-}$ dissolution energies. (b) $\text{P}_2\text{S}_7^{4-}$ reaction A energies forming $\text{P}_2\text{S}_6^{4-}$ and S^{2-} . (c) $\text{P}_2\text{S}_7^{4-}$ and S^{2-} reaction B energies forming PS_4^{3-} . Calculation details can be found in the [Experimental Section](#).

This suggests that PS_4^{3-} formation is driven by a combination of S^{2-} formation from the first reaction A (favored by higher dielectric constants) and the subsequent reaction B of that intermediate to form PS_4^{3-} (favored by low dielectric constants). This explains why an increase in the intensity for PS_4^{3-} is observed in an intermediate dielectric constant DMC; lower dielectric constant solvents such as TOL and XYL would limit S^{2-} formation, while higher dielectric constant solvents such as ACN would inhibit PS_4^{3-} formation. These indicate that conductive and crystalline properties of $\text{Li}_7\text{P}_3\text{S}_{11}$ can be retained by using solvents with relatively low dielectric constants such as TOL and XYL.

These findings are validated by the EIS measurements (Figure 5) of SSE powders collected after the solvent removal. Specifically, the precipitates from ACN and DMC solvent mixtures showed a loss of 2–3 orders of magnitude in conductivities, at 7.4×10^{-7} and 1.1×10^{-5} S cm^{-1} , respectively (Table 2). This results from a large charge transfer resistance represented by the semicircle feature in the Nyquist plots of ACN and DMC dispersed SSE powders (Figure 5). This is expected as the decomposed products of PS_4^{3-} and $\text{P}_2\text{S}_6^{4-}$ formed are either poor conductors or insulative in nature, contributing to increased resistance of the electrolyte. By contrast, the conductivities of precipitates from TOL and XYL measured at 1.12×10^{-3} and 1.19×10^{-3} S cm^{-1} , respectively, retain almost all the pristine conductivity of 1.2×10^{-3} S cm^{-1} .

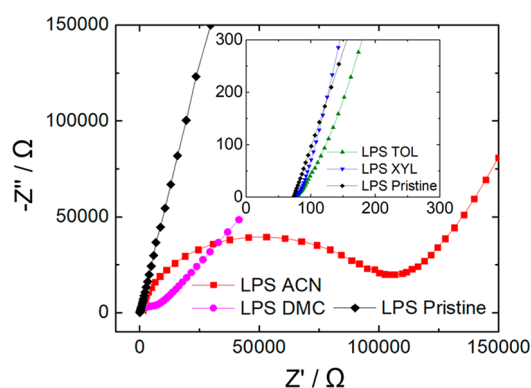


Figure 5. Nyquist plots of $\text{Li}_7\text{P}_3\text{S}_{11}$ EIS measurements after dispersion in different solvents, showing large charge transfer resistances from ACN and DMC dispersions. The high-frequency inset shows TOL and XYL dispersions.

Table 2. Conductivity Measurements of $\text{Li}_7\text{P}_3\text{S}_{11}$ after Dispersion in Different

solvent	conductivity/ S cm^{-1}
pristine	1.20×10^{-3}
XYL	1.19×10^{-3}
TOL	1.12×10^{-3}
DMC	1.11×10^{-5}
ACN	7.4×10^{-7}

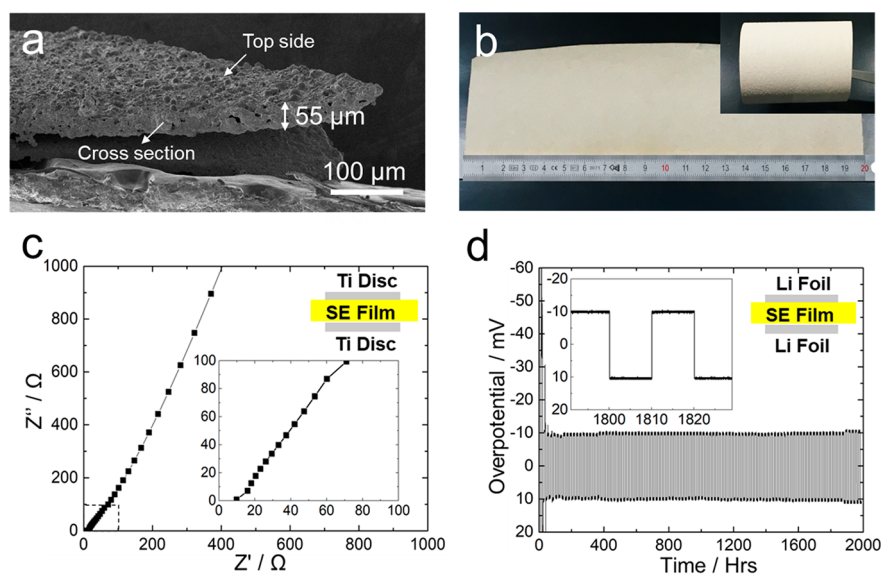


Figure 6. (a) Cross-section SEM image of composite electrolyte film fabricated with 95 wt % $\text{Li}_7\text{P}_3\text{S}_{11}$ and 5 wt % SEBS. (b) Digital photograph of a 20 cm \times 6 cm casted electrolyte film and a rolled-up film (inset). (c) Nyquist plot of the composite electrolyte film. (d) Li plating and stripping across composite electrolyte film with 100 cycles at 20 h per cycle. The inset shows the setup used. All measurements were done at room temperature.

From the characterization study, it is clear that solvent selection is crucial to the performance of composite electrolytes. Chemical degradation was observed in $\text{Li}_7\text{P}_3\text{S}_{11}$ when dispersed in polar solvents with high dielectric constants such as ACN and DMC, while chemical structure and ionic conductivities were retained when nonpolar solvents with low dielectric constant such as TOL and XYL were used.

$\text{Li}_7\text{P}_3\text{S}_{11}$ –Polymer Compatibility. To examine effects of polymer on the composite electrolyte, $\text{Li}_7\text{P}_3\text{S}_{11}$ and respective polymers including PEO, PVDF-HFP, NBR, and SEBS were mixed and characterized. A 50:50 wt % ratio was used to ensure excess of polymer in the mixtures to exaggerate any potential reactions observed. However, no reactions or electrolyte degradation was detected in the SSE–polymer mixtures. The Raman spectra of all mixtures retained both peak positions and relative intensities of lithium thiophosphate modes $\text{P}_2\text{S}_7^{4-}$, PS_4^{3-} , and $\text{P}_2\text{S}_6^{4-}$ (Figure S3), indicating retention of the local structures of $\text{Li}_7\text{P}_3\text{S}_{11}$. XPS analysis was also conducted to identify any new phosphorus and sulfur products formed as a result of any side reactions in each mixture. Consistent with the Raman analysis, no new reaction or decomposition products were detected by XPS (Figure S4). The characteristic peak patterns matched the pristine counterparts in both the phosphorus and sulfur regions, comprising the main components of $\text{P}_2\text{S}_7^{4-}$ and PS_4^{3-} . As a result, we are not able to detect any chemical reactions or electrolyte decomposition from the dry mixtures of $\text{Li}_7\text{P}_3\text{S}_{11}$ and the respective polymers. However, this analysis does not account for other potential interactions such as localized electrostatic interactions or coordination between the nucleophilic phosphorus groups in the SSE and electronegative oxygen or fluorine groups in polymers. While it is also important to study such behavior to understand their physical behavior, we will focus instead on the chemical and electrochemical effects since they ultimately determine the composite electrolyte's properties. Accordingly, suitable polymer–solvent pairs include polymers with weak or no electronegative groups which can be readily dispersed in nonpolar solvents with low dielectric

constants. From the analysis, SEBS polymer and *p*-xylene appear to be a suitable choice.

Electrochemical Evaluation of $\text{Li}_7\text{P}_3\text{S}_{11}$ –Polymer Composite. Composite films of $\text{Li}_7\text{P}_3\text{S}_{11}$ and SEBS were fabricated by casting slurries with XYL as the solvent. The thickness of the composite electrolyte films can be controlled at $\sim 50 \mu\text{m}$ or less (Figure 6a). For this study, all composites were synthesized with 5 wt % of polymer to minimize variables. A lower weight percent of polymer may be used to optimize the electrochemical performance in future studies. With this composition, large area composite electrolyte films can be fabricated (Figure 6b). The flexibility of composite film is demonstrated in Movie S1. The fabricated composite film electrolyte's room temperature conductivity was evaluated via electrochemical impedance spectroscopy (EIS) (Figure 6a). Titanium blocking electrodes were used in the test, which measured resistances of 10 ohm across the $55 \mu\text{m}$ thick film (Figure 6), translating to an area-specific resistance of $3.9 \Omega \text{ cm}^2$.

Its conductivity was calculated to be 0.7 mS cm^{-1} , which is within the expected conductivity loss from pure $\text{Li}_7\text{P}_3\text{S}_{11}$ at 1.2 mS cm^{-1} . Conductivity losses are expected to vary based on the composition and can be minimized with further reductions in polymer wt %. Addition of polymer into the composite also introduced extra porosity into the matrix; the pores are nonconductive and contribute to resistance of the film. However, despite losses in specific conductivity, the significant reduction (>1 order) in electrolyte thickness can still give rise to dramatic decrease in the overall resistance compared to the bulk pristine electrolyte pellets. While EIS measurements can provide a quantitative understanding of electrolyte conductivity based on charge transfer, its limitations include the inability to provide qualitative information such as the identity of the conducting species. To ensure no other components such as proton species or water adsorption influenced the measurements, nonblocking electrodes were also used. Plating and stripping were performed with 20 h per cycle by using a current of 0.11 mA cm^{-2} at room temperature. The electrolyte

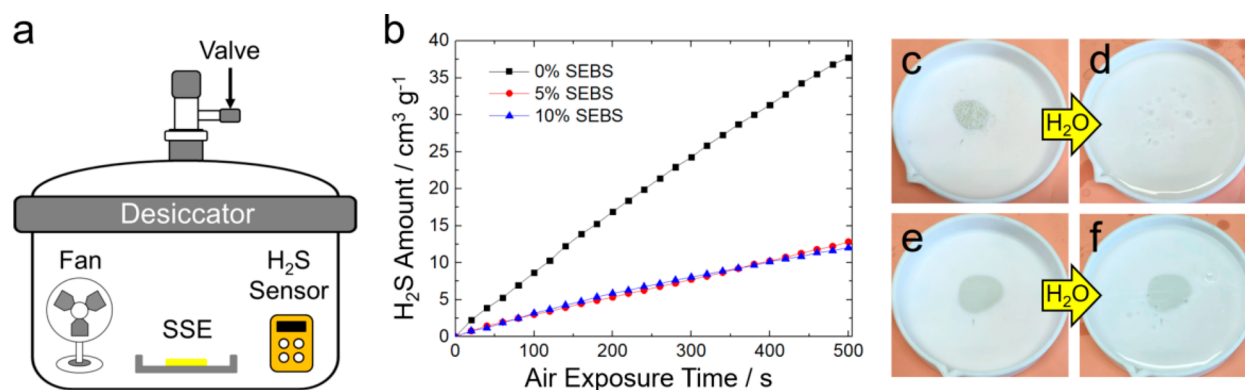


Figure 7. (a) Setup used for H₂S gas measurements from 100 mg of Li₇P₃S₁₁ hydrolysis in air. (b) H₂S amount released vs time for fixed volume air exposed to 100 mg of bare Li₇P₃S₁₁ and 100 mg of composite with hydrophobic SEBS polymer. (c, d) Bare Li₇P₃S₁₁ before and after flooding in water, showing full hydrolysis and disappearance in water. (d, e) Composite electrolyte film before and after flooding in water, showing retention of the film.

film was found to remain stable over 2000 h of cycling, with a measured overpotential of 10 mV. It is observed that the plating overpotential of the symmetric cell was high initially and stabilized after several cycles. This can be attributed to the poor dotted contact between Li foil and the fresh surface of the electrolyte film at the initial stage. We hypothesize that as plating and stripping proceed, the gaps gradually become filled, and the contact is improved over extended cycling, allowing plating overpotentials to stabilize.

Air/Moisture Stability Test. The hydrophobicity of each polymer used was first compared by measuring their contact angles with water (Figure S7). SEBS was found to be the most hydrophobic polymer (with a contact angle of 103°) in the study. Subsequently, moisture stability in air of the composite electrolyte was tested based on the quantity of H₂S evolved during air exposure of Li₇P₃S₁₁ (Figure 7a). The use of hydrophobic SEBS in the composite electrolyte was found to significantly improve the film's moisture stability in air with a relative humidity of 50–55% compared to the bare Li₇P₃S₁₁ powder. Using 5 wt % of SEBS in the composite electrolyte, we observed considerably reduced H₂S evolution compared with bare Li₇P₃S₁₁ samples under the same exposure condition (Figure 7b).

To further examine the effects of moisture on the electrolyte stability, distilled water was gradually added to a dish containing 100 mg of bare electrolyte and the composite electrolyte film (Movie S2). From Figures 7c and 7d, it is observed that the bare electrolyte completely degraded upon contact with water, while the composite electrolyte film remained intact despite being fully submerged in water (Figures 7e and 7f). This result indicates that use of hydrophobic polymers can help to stabilize the water-sensitive Li₇P₃S₁₁ electrolyte in moisture, potentially improving the processability of sulfide-based electrolytes in dry room conditions if other superhydrophobic materials can be used.

CONCLUSION

In summary, this study seeks to elucidate various polymer and solvent interactions and their compatibilities with a representative sulfide solid electrolyte. We demonstrated that by using an SSE such as Li₇P₃S₁₁, in combination with nonpolar solvents of low dielectric constant such as *p*-xylene and a corresponding polymer without electronegative functional groups such as SEBS, highly conductive (~0.7 mS cm⁻¹)

thin electrolyte films (~50 μm) with good mechanical properties can be fabricated. The composite electrolyte film was also found to be electrochemically stable with lithium over long cycles of plating and stripping (2000 h, 1.1 mAh cm⁻² per cycle), potentially enabling the use of metallic lithium anode in ASSBs. Moreover, the use of hydrophobic SEBS was also found to improve moisture stability of Li₇P₃S₁₁ in air. The principles of SSE–polymer–solvent selection found in this study can be further extended to other SSE–polymer–solvent compositions and optimized to achieve better performance. Additionally, the knowledge gained in this study may provide new material selection philosophy and lead to development of future scalable methods to produce high-performance, low-cost ASSBs.

EXPERIMENTAL SECTION

Glass Ceramic Synthesis. Li₇P₃S₁₁ was synthesized by using the melt quench process developed in an earlier study.²⁵ Precursors Li₂S (99.98%, Sigma-Aldrich) and P₂S₅ (99%, Sigma-Aldrich) were mixed in an agate mortar and pestle for 15 min in the following stoichiometric ratio: 70Li₂S:30P₂S₅. Once mixed, the powder was vacuum-sealed in a quartz tube. The sealed tube was heated to 750 °C over a period of 4 h, with 1.5 h of ramping time. Subsequently, the tube was quickly quenched in an ice bath. Upon cooling, the glassy SSE powder was once again mixed in an agate mortar and pestle for 15 min, sealed in a vacuum quartz tube. The sealed tube was then placed in a preheated furnace at 300 °C for 2 h. Subsequently, the tube was quickly removed from the box furnace and quenched in an ice bath. Upon cooling, the final glass ceramic Li₇P₃S₁₁ was grinded in an agate mortar and pestle for 15 min before use.

Preparation of SSE–Solvent/Polymer Mixtures for Characterization. All solvents and polymers were obtained from Sigma-Aldrich. Solvents used were in anhydrous forms or dried with molecular sieves. Polymer powders were first dried in a heated vacuum oven before use. To prepare sulfide/polymer mixtures, the as-synthesized Li₇P₃S₁₁ powder was mixed with different polymers in a vial at a 50:50 wt ratio. The vial was mixed in an ARM 310 Thinky mixer for 3 min at 2000 rpm and allowed to rest for 1 day before characterization. To prepare the sulfide/solvent mixtures, equal amounts of as-synthesized SSE powder were added to 5 mL of each solvent. The mixtures were hand-swirled briefly to disperse the powders before allowing to rest for 1 h. Subsequently, the solvents were removed by heating at 60 °C under vacuum overnight to obtain the residual solutes. To eliminate air exposure, all samples were collected and prepared in an argon-filled environment.

Composite Film Casting. In a typical experiment, 250 mg of SEBS polymer was added to 10 mL of solvent. The vial was capped and left to stir until the polymer was fully dissolved. To prepare the

electrolyte slurry, SSE was first weighed into a Thinky mixer vial before the polymer solution was added. The vial was then capped and sealed to prevent air exposure before mixing for 3 min under 2000 rpm. After mixing, the slurry was casted with a doctor blade and left to dry at room temperature for 1 h and overnight at 60 °C under vacuum. Casting was done either on an aluminum current collector or a Teflon plate. The dried films cut from the current collector or peeled from the Teflon plates were pressed under 370 MPa of pressure for at least 3 min before use.

Air Stability Evaluation. The amount of H₂S gas generated from the composite electrolyte film due to reaction with moisture in air was measured. A H₂S gas monitor (SensorCon, Industrial Pro), a fan, and the electrolyte film were sealed in an air-filled 0.31 ft³ desiccator (Bell-Art Products). The air temperature was 22–24 °C with a relative humidity between 50 and 55%. Measurements were taken from the H₂S gas monitor over a period of 10 min and compared against 100 mg of bare Li₇P₃S₁₁ electrolyte. The contact angle of each polymer was collected by using a Rame Hart goniometer and measured with a DROPimage Advanced tool.

Materials Characterization. X-ray diffraction (XRD) was conducted by using Cu K α radiation ($\lambda = 1.54178$) over a 2θ range of 5°–70° with a step size of 0.01°. XRD Rietveld crystal refinement was conducted by using the Full-Prof software, and the lattice parameters were reported. A PerkinElmer RamanStation 400F spectrometer was used to collect Raman spectra intensity values from 134 to 1500 cm⁻¹. Raman spectra were then deconvoluted with a range of 350 and 455 cm⁻¹ using least-squares fitting. A FEI Quanta 250 scanning electron microscope was used to characterize the film thickness as well as surface morphology. Thickness of films were noted using the cross-section measurement tool. The AXIS Supra XPS by Kratos Analytical was used to study the chemical degradation of Li₇P₃S₁₁ when exposed to the various polymers and solvents. Binding energies of the mixtures in the phosphorus and sulfur regions were examined against pristine Li₇P₃S₁₁. The XPS spectra were collected by using an emission current of 5 mA and over an area of 700 $\mu\text{m} \times 300 \mu\text{m}$. The spectra were analyzed by using CasaXPS software.

Electrochemical Characterization. EIS measurements were performed with a Solartron 1260 impedance analyzer for the pristine SSE, synthesized electrolyte films, and precipitates derived from different solvents. An applied ac potential of 30 mV over a frequency range from 1 MHz to 1 Hz was used for the EIS measurement. The composite films were pressed at 370 MPa before being cut into circular discs and placed between two titanium blocking electrodes for measurements. In the symmetric cells, Li foils were placed on both sides of the free-standing film, and lithium plating and stripping were conducted across the film.

Density Functional Theory (DFT) Calculations. The solvation and reaction energies of sulfur and thiophosphate anions are calculated by using the Gaussian 09 quantum chemistry package.³⁷ The hybrid B3LYP density functional based on Becke's three-parameter exchange functional³⁸ and the correlation functional of Lee, Yang, and Parr³⁹ were chosen for all calculations. Geometry optimizations were performed at the B3LYP/6-31+G(d) level, followed by single-point energy calculations at the B3LYP/6-311+G(2d,p) level. The inclusion of diffuse functions in the basis sets ensures an adequate description of the diffuse electron cloud of anions. An SMD solvation model is adopted for all calculations involving solvents.⁴⁰

■ ASSOCIATED CONTENT

● Supporting Information

The Supporting Information is available free of charge on the ACS Publications website at DOI: 10.1021/acsaem.9b01111.

Electrolyte composite characterization (XRD refinement, Raman analysis, Nyquist plot, XPS), polymer FTIR, polymer solvent dispersion, polymer hydrophobicity, full cell performance, table of summarized

composite electrolytes in the literature, table of polymers and solvents with structures (PDF)

Movie S1: flexibility of composite film (MP4)

Movie S2: effects of moisture on composite film (MP4)

■ AUTHOR INFORMATION

Corresponding Authors

*E-mail shmeng@ucsd.edu.

*E-mail zhengchen@eng.ucsd.edu.

ORCID

Shyue Ping Ong: 0000-0001-5726-2587

Ying Shirley Meng: 0000-0001-8936-8845

Zheng Chen: 0000-0002-9186-4298

Notes

The authors declare the following competing financial interest(s): A patent was filed for this work through the UCSD Office of Innovation and Commercialization.

■ ACKNOWLEDGMENTS

This study was financially supported by the LG Chem through Battery Innovation Contest (BIC) program. The authors acknowledge the UCSD Crystallography Facility. This work was performed in part at the San Diego Nanotechnology Infrastructure (SDNI) of UCSD, a member of the National Nanotechnology Coordinated Infrastructure, which is supported by the National Science Foundation (Grant ECCS-1542148).

■ ABBREVIATIONS

ACN, acetonitrile; ASSBs, all-solid-state batteries; DFT, density functional theory; DMC, dimethyl carbonate; DMF, dimethylformamide; EIS, electrochemical impedance spectroscopy; NBR, acrylonitrile butadiene; NMP, *N*-methyl-2-pyrrolidone; MEK, methyl ethyl ketone; PEO, poly(ethylene oxide); PLD, pulsed laser deposition; PVDF(HFP), poly(vinylidene fluoride)-(cohexafluoropropylene); PVD, pulsed vapor deposition; PVP, polyvinylpyrrolidone; SEBS, polystyrene-*block*-poly(ethylene-*ran*-butylene)-*block*-polystyrene; SEM, scanning electron microscope; SSEs, solid state electrolytes; THF, tetrahydrofuran; TOL, toluene; XPS, X-ray photoelectron spectroscopy; XRD, X-ray diffraction; XYL, xylene.

■ REFERENCES

- Jung, Y. S.; Oh, D. Y.; Nam, Y. J.; Park, K. H. Issues and Challenges for Bulk-Type All-Solid-State Rechargeable Lithium Batteries using Sulfide Solid Electrolytes. *Isr. J. Chem.* **2015**, *55* (5), 472–485.
- Kerman, K.; Luntz, A.; Viswanathan, V.; Chiang, Y.-M.; Chen, Z. Review—Practical Challenges Hindering the Development of Solid State Li Ion Batteries. *J. Electrochem. Soc.* **2017**, *164* (7), A1731–A1744.
- Zhai, H.; Xu, P.; Ning, M.; Cheng, Q.; Mandal, J.; Yang, Y. A Flexible Solid Composite Electrolyte with Vertically Aligned and Connected Ion-Conducting Nanoparticles for Lithium Batteries. *Nano Lett.* **2017**, *17* (5), 3182–3187.
- Fan, X.; Ji, X.; Han, F.; Yue, J.; Chen, J.; Chen, L.; Deng, T.; Jiang, J.; Wang, C. Fluorinated solid electrolyte interphase enables highly reversible solid-state Li metal battery. *Sci. Adv.* **2018**, *4*, No. eaau9245.
- Kasemchainan, J.; Bruce, P. G. All-Solid-State Batteries and their Remaining Challenges. *Johnson Matthey Technol. Rev.* **2018**, *62* (2), 177–180.

- (6) Schnell, J.; Günther, T.; Knoche, T.; Vieider, C.; Köhler, L.; Just, A.; Keller, M.; Passerini, S.; Reinhart, G. All-solid-state lithium-ion and lithium metal batteries – paving the way to large-scale production. *J. Power Sources* **2018**, *382*, 160–175.
- (7) Porz, L.; Swamy, T.; Sheldon, B. W.; Rettenwander, D.; Frömling, T.; Thaman, H. L.; Berendts, S.; Uecker, R.; Carter, W. C.; Chiang, Y.-M. Mechanism of Lithium Metal Penetration through Inorganic Solid Electrolytes. *Adv. Energy Mater.* **2017**, *7* (20), 1701003.
- (8) Park, K. H.; Bai, Q.; Kim, D. H.; Oh, D. Y.; Zhu, Y.; Mo, Y.; Jung, Y. S. Design Strategies, Practical Considerations, and New Solution Processes of Sulfide Solid Electrolytes for All-Solid-State Batteries. *Adv. Energy Mater.* **2018**, *8* (18), 1800035.
- (9) Sakuda, A.; Hayashi, A.; Takigawa, Y.; Higashi, K.; Tatsumisago, M. Evaluation of elastic modulus of $\text{Li}_2\text{S}\cdot\text{P}_2\text{S}_5$ glassy solid electrolyte by ultrasonic sound velocity measurement and compression test. *J. Ceram. Soc. Jpn.* **2013**, *121* (1419), 946–949.
- (10) Sakuda, A.; Hayashi, A.; Tatsumisago, M. Sulfide solid electrolyte with favorable mechanical property for all-solid-state lithium battery. *Sci. Rep.* **2013**, *3*, 2261.
- (11) Kato, Y.; Shiotani, S.; Morita, K.; Suzuki, K.; Hirayama, M.; Kanno, R. All-Solid-State Batteries with Thick Electrode Configurations. *J. Phys. Chem. Lett.* **2018**, *9* (3), 607–613.
- (12) Busche, M. R.; Weber, D. A.; Schneider, Y.; Dietrich, C.; Wenzel, S.; Leichtweiss, T.; Schroder, D.; Zhang, W.; Weigand, H.; Walter, D.; Sedlmaier, S. J.; Houtarde, D.; Nazar, L. F.; Janek, J. In Situ Monitoring of Fast Li-Ion Conductor $\text{Li}_7\text{P}_3\text{S}_{11}$ Crystallization Inside a Hot-Press Setup. *Chem. Mater.* **2016**, *28* (17), 6152–6165.
- (13) Cheng, L.; Crumlin, E. J.; Chen, W.; Qiao, R.; Hou, H.; Franz Lux, S.; Zorba, V.; Russo, R.; Kostecky, R.; Liu, Z.; Persson, K.; Yang, W.; Cabana, J.; Richardson, T.; Chen, G.; Doeff, M. The origin of high electrolyte-electrode interfacial resistances in lithium cells containing garnet type solid electrolytes. *Phys. Chem. Chem. Phys.* **2014**, *16* (34), 18294–18300.
- (14) Sakuda, A.; Hayashi, A.; Hama, S.; Tatsumisago, M. Preparation of Highly Lithium-Ion Conductive $80\text{Li}_2\text{S}\cdot20\text{P}_2\text{S}_5$ Thin-Film Electrolytes Using Pulsed Laser Deposition. *J. Am. Ceram. Soc.* **2010**, *93* (3), 765–768.
- (15) Tao, X.; Liu, Y.; Liu, W.; Zhou, G.; Zhao, J.; Lin, D.; Zu, C.; Sheng, O.; Zhang, W.; Lee, H. W.; Cui, Y. Solid-State Lithium-Sulfur Batteries Operated at 37 °C with Composites of Nanostructured $\text{Li}_7\text{La}_3\text{Zr}_2\text{O}_{12}$ /Carbon Foam and Polymer. *Nano Lett.* **2017**, *17* (5), 2967–2972.
- (16) Zheng, J.; Tang, M.; Hu, Y. Y. Lithium Ion Pathway within $\text{Li}_7\text{La}_3\text{Zr}_2\text{O}_{12}$ -Polyethylene Oxide Composite Electrolytes. *Angew. Chem., Int. Ed.* **2016**, *55* (40), 12538–12542.
- (17) Guo, Q.; Han, Y.; Wang, H.; Xiong, S.; Li, Y.; Liu, S.; Xie, K. New Class of LAGP-Based Solid Polymer Composite Electrolyte for Efficient and Safe Solid-State Lithium Batteries. *ACS Appl. Mater. Interfaces* **2017**, *9* (48), 41837–41844.
- (18) Choi, J.-H.; Lee, C.-H.; Yu, J.-H.; Doh, C.-H.; Lee, S.-M. Enhancement of ionic conductivity of composite membranes for all-solid-state lithium rechargeable batteries incorporating tetragonal $\text{Li}_7\text{La}_3\text{Zr}_2\text{O}_{12}$ into a polyethylene oxide matrix. *J. Power Sources* **2015**, *274*, 458–463.
- (19) Zhang, X.; Liu, T.; Zhang, S.; Huang, X.; Xu, B.; Lin, Y.; Xu, B.; Li, L.; Nan, C. W.; Shen, Y. Synergistic Coupling between $\text{Li}_{6.7}\text{La}_3\text{Zr}_{1.75}\text{Ta}_{0.25}\text{O}_{12}$ and Poly(vinylidene fluoride) Induces High Ionic Conductivity, Mechanical Strength, and Thermal Stability of Solid Composite Electrolytes. *J. Am. Chem. Soc.* **2017**, *139* (39), 13779–13785.
- (20) Lee, K.; Kim, S.; Park, J.; Park, S. H.; Coskun, A.; Jung, D. S.; Cho, W.; Choi, J. W. Selection of Binder and Solvent for Solution-Processed All-Solid-State Battery. *J. Electrochem. Soc.* **2017**, *164* (9), A2075–A2081.
- (21) Nam, Y. J.; Oh, D. Y.; Jung, S. H.; Jung, Y. S. Toward practical all-solid-state lithium-ion batteries with high energy density and safety: Comparative study for electrodes fabricated by dry- and slurry-mixing processes. *J. Power Sources* **2018**, *375*, 93–101.
- (22) Shao, C.; Liu, H.; Yu, Z.; Zheng, Z.; Sun, N.; Diao, C. Structure and ionic conductivity of cubic $\text{Li}_7\text{La}_3\text{Zr}_2\text{O}_{12}$ solid electrolyte prepared by chemical co-precipitation method. *Solid State Ionics* **2016**, *287*, 13–16.
- (23) McCloskey, B. D. Attainable gravimetric and volumetric energy density of Li-S and Li ion battery cells with solid separator-protected Li metal anodes. *J. Phys. Chem. Lett.* **2015**, *6* (22), 4581–8.
- (24) Agrawal, R. C.; Pandey, G. P. Solid polymer electrolytes: materials designing and all-solid-state battery applications: an overview. *J. Phys. D: Appl. Phys.* **2008**, *41* (22), 223001.
- (25) Chu, I. H.; Nguyen, H.; Hy, S.; Lin, Y. C.; Wang, Z.; Xu, Z.; Deng, Z.; Meng, Y. S.; Ong, S. P. Insights into the Performance Limits of the $\text{Li}_7\text{P}_3\text{S}_{11}$ Superionic Conductor: A Combined First-Principles and Experimental Study. *ACS Appl. Mater. Interfaces* **2016**, *8* (12), 7843–53.
- (26) Yao, X.; Liu, D.; Wang, C.; Long, P.; Peng, G.; Hu, Y. S.; Li, H.; Chen, L.; Xu, X. High-Energy All-Solid-State Lithium Batteries with Ultralong Cycle Life. *Nano Lett.* **2016**, *16* (11), 7148–7154.
- (27) Wenzel, S.; Weber, D. A.; Leichtweiss, T.; Busche, M. R.; Sann, J.; Janek, J. Interphase formation and degradation of charge transfer kinetics between a lithium metal anode and highly crystalline $\text{Li}_7\text{P}_3\text{S}_{11}$ solid electrolyte. *Solid State Ionics* **2016**, *286*, 24–33.
- (28) Jeschull, F.; Maibach, J.; Edström, K.; Brandell, D. On the Electrochemical Properties and Interphase Composition of Graphite: PVdF-HFP Electrodes in Dependence of Binder Content. *J. Electrochem. Soc.* **2017**, *164* (7), A1765–A1772.
- (29) Peled, E.; Goor, M.; Schektman, I.; Mukra, T.; Shoval, Y.; Golodnitsky, D. The Effect of Binders on the Performance and Degradation of the Lithium/Sulfur Battery Assembled in the Discharged State. *J. Electrochem. Soc.* **2017**, *164* (1), A5001–A5007.
- (30) Le, A. V.; Wang, M.; Noelle, D. J.; Shi, Y.; Shirley Meng, Y.; Wu, D.; Fan, J.; Qiao, Y. Using high-HFP-content cathode binder for mitigation of heat generation of lithium-ion battery. *Int. J. Energy Res.* **2017**, *41* (14), 2430–2438.
- (31) Lacey, M. J.; Jeschull, F.; Edstrom, K.; Brandell, D. Why PEO as a binder or polymer coating increases capacity in the Li-S system. *Chem. Commun.* **2013**, *49* (76), 8531–3.
- (32) Yamane, H.; Shibata, M.; Shimane, Y.; Junke, T.; Seino, Y.; Adams, S.; Minami, K.; Hayashi, A.; Tatsumisago, M. Crystal structure of a superionic conductor, $\text{Li}_7\text{P}_3\text{S}_{11}$. *Solid State Ionics* **2007**, *178* (15–18), 1163–1167.
- (33) Wang, Y.; Lu, D.; Bowden, M.; El Khoury, P. Z.; Han, K. S.; Deng, Z. D.; Xiao, J.; Zhang, J.-G.; Liu, J. Mechanism of Formation of $\text{Li}_7\text{P}_3\text{S}_{11}$ Solid Electrolytes through Liquid Phase Synthesis. *Chem. Mater.* **2018**, *30* (3), 990–997.
- (34) Calpa, M.; Rosero-Navarro, N. C.; Miura, A.; Tadanaga, K. Nataly Carolina Miura, Akira Tadanaga, Kiyoharu, Instantaneous preparation of high lithium-ion conducting sulfide solid electrolyte $\text{Li}_7\text{P}_3\text{S}_{11}$ by a liquid phase process. *RSC Adv.* **2017**, *7* (73), 46499–46504.
- (35) Xu, R. C.; Xia, X. H.; Yao, Z. J.; Wang, X. L.; Gu, C. D.; Tu, J. P. Preparation of $\text{Li}_7\text{P}_3\text{S}_{11}$ glass-ceramic electrolyte by dissolution-evaporation method for all-solid-state lithium ion batteries. *Electrochim. Acta* **2016**, *219*, 235–240.
- (36) Lim, H.-D.; Lim, H.-K.; Xing, X.; Lee, B.-S.; Liu, H.; Coaty, C.; Kim, H.; Liu, P. Solid Electrolyte Layers by Solution Deposition. *Adv. Mater. Interfaces* **2018**, *5* (8), 1701328.
- (37) Frisch, M. J.; Trucks, G. W.; Schlegel, H. B.; Scuseria, G. E.; Robb, M. A.; Cheeseman, J. R.; Scalmani, G.; Barone, V.; Mennucci, B.; Petersson, G. A.; Nakatsuji, H.; Caricato, M.; Li, X.; Hratchian, H. P.; Izmaylov, A. F.; Bloino, J.; Zheng, G.; Sonnenberg, J. L.; Hada, M.; Ehara, M.; Toyota, K.; Fukuda, R.; Hasegawa, J.; Ishida, M.; Nakajima, T.; Honda, Y.; Kitao, O.; Nakai, H.; Vreven, T.; Montgomery, J. A., Jr.; Peralta, J. E.; Ogliaro, F.; Bearpark, M.; Heyd, J. J.; Brothers, E.; Kudin, K. N.; Staroverov, V. N.; Keith, T.; Kobayashi, R.; Normand, J.; Raghavachari, K.; Rendell, A.; Burant, J. C.; Iyengar, S. S.; Tomasi, J.; Cossi, M.; Rega, N.; Millam, J. M.; Klene, M.; Knox, J. E.; Cross, J. B.; Bakken, V.; Adamo, C.; Jaramillo, J.; Gomperts, R.; Stratmann, R. E.; Yazyev, O.; Austin, A. J.; Cammi,

R.; Pomelli, C.; Ochterski, J. W.; Martin, R. L.; Morokuma, K.; Zakrzewski, V. G.; Voth, G. A.; Salvador, P.; Dannenberg, J. J.; Dapprich, S.; Daniels, A. D.; Farkas, O.; Foresman, J. B.; Ortiz, J. V.; Cioslowski, J.; Fox, D. J. *Gaussian 09*, Revision A.02; Gaussian, Inc.: Wallingford, CT, 2013.

(38) Becke, A. D. Density-functional thermochemistry. III. The role of exact exchange. *J. Chem. Phys.* **1993**, *98* (7), 5648–5652.

(39) Lee, C.; Yang, W.; Parr, R. G. Development of the Colle-Salvetti correlation-energy formula into a functional of the electron density. *Phys. Rev. B: Condens. Matter Mater. Phys.* **1988**, *37* (2), 785–789.

(40) Marenich, A. V.; Cramer, C. J.; Truhlar, D. G. Universal Solvation Model Based on Solute Electron Density and on a Continuum Model of the Solvent Defined by the Bulk Dielectric Constant and Atomic Surface Tensions. *J. Phys. Chem. B* **2009**, *113* (18), 6378–6396.